RSC Advances

ROYAL SOCIETY OF CHEMISTRY

www.rsc.org/advances

Engineering the NiO/CeO_2 interface to enhance the catalytic performance for CO oxidation

Weixin Zou,[a,b†] Chengyan Ge,[c†] Minyue Lu,[a,b] Shiguo Wu,[a,b] Yongzheng Wang,[a] Jingfang Sun,[b] Yu Pu,[a] Changjin Tang,[a,b] Fei Gao,*[a,b] Lin Dong*[a,b]

[a] Key Laboratory of Mesoscopic Chemistry of MOE, School of Chemistry and Chemical Engineering, Nanjing University, Nanjing 210093, PR China

[b] Jiangsu Key Laboratory of Vehicle Emissions Control, Center of Modern Analysis, Nanjing University, Nanjing 210093, PR China

[c] School of Chemistry and Chemical Engineering, Yancheng Institute of Technology, Yanchen 224051, PR China

† These authors contribute equally.

Corresponding Author

*E-mail: gaofei@nju.edu.cn, donglin@nju.edu.cn Tel: +86-25-83592290 Fax: +86-25-83317761

ABSTRACT: In this work, NiO/CeO_2 catalysts were synthesized with tunable CeO_2 crystal facets ({110}, {111} and {100} facets) to study the crystal-plane effects on the catalytic properties. Kinetic studies of CO oxidation showed that NiO/CeO_2 {110} had the lowest activation energy. Furthermore, the obtained samples were characterized by means of TEM, XRD, Raman, N_2-physisorption, UV-Vis DRS, XPS, H_2-TPR and *in-situ* DRIFTS technologies. The results demonstrated that the geometric and electronic structures of nickel species were dependent on the NiO/CeO_2 interfaces, which had an influence on the synergetic interaction of absorbed CO and active oxygen species, and then the generation of the formate intermediate played an important role in the catalytic performance. The possible interface structures of nickel species on the CeO_2 {110}, {111} and {100} surface were proposed through the incorporation model, suggesting that the advantageous NiO/CeO_2{110} interface was facilitate for CO adsorption/activation and active oxygen species formation, leading to the best catalytic performance.

KEYWORDS: *crystal-plane effect, NiO/CeO_2, CO oxidation, in-situ DRIFTS, interfacial interaction*

1. INTRODUCTION

Cerium oxide and ceria-based materials have received increasing attentions and intensively studied in environmental catalysis,[1-3] due to the rich oxygen vacancy and high oxygen storage-release capacity (OSC) in Ce^{4+}/Ce^{3+} redox cycle.[4,5] Furthermore, thanks to the advantage of shape-controlled synthesis, the ceria nanocrystals with specific exposure facets, such as rods with {110} facets, octahedrons with {111} facets and cubes with {100} facets, have attracted considerable research interest.[6,7] Theoretical and experimental studies have demonstrated that the properties of ceria-based nanocrystals are affected by the surface structures of different exposed crystal facets.[8-11] Nolan *et al.* proposed that the oxygen vacancy formation energy of CeO_2 was surface sensitive by theoretical calculation, in the order of {110} < {100} < {111}.[8] And the stability of CeO_2 was closely related to the crystal facets. It was showed that the CeO_2 {111} facet was provided with the lowest surface energy, {110} facet was followed, and {100} facet had the highest surface energy.[9,10] Extensive studies have been devoted to exploring the structure-effects of ceria nanocrystals on CO oxidation.[12,13] Wang *et al.* compared the activity of CeO_2 cube and truncated octahedron in CO oxidation, and found that the cube displayed the enhanced activity, due to the existence of more coordinatively unsaturated cerium atoms and active adsorption oxygen species on the CeO_2 {100} surface.[12]

Moreover, it is reached a general consensus that the strong metal-support interaction (SMSI) is the key factor for the catalytic performances.[14,15] Flytzani-Stephanopoulos *et al.* studied the crystal-plane effects of CeO_2 nanocrystals on the Au/CeO_2 for the water-gas shift (WGS) reaction, and discovered that ceria rods with {110} planes were most active for gold stabilization/activation.[16] Similarly, between the oxide-oxide interface, the interactions also play an important role in catalysis. Our previous work had presented that the crystal planes of CeO_2 nanocrystals made a great influence on the CuO/CeO_2 catalysts for NO+CO reaction, we found that the synergistic interactions between CuO and CeO_2 rods were intensified, leading to the superior performances.[17] In addition, nickel oxide, with

excellent redox property, has been attempted to combine with ceria. The addition of NiO into ceria can generally increase the concentration of oxygen vacancies and enhance the oxygen diffusion of ceria, which contributes to superior performance in many reactions.[18,19] Zhou *et al.* prepared a series of NiCe mixed oxides for the catalytic N_2O decomposition, and found that the strong interaction between NiO and CeO_2 resisted the inhibition of O_2 and enhanced the oxygen mobility.[20] However, in literature, most of the NiO/CeO_2 catalysts are irregularly shaped, without the well-defined crystal facets exposed. On the basis that the different CeO_2 nanostructures affect the geometric and electronic states of nickel species on the interface, the oxide-oxide interfacial interaction of NiO/CeO_2 catalysts is worthy of study.

Therefore, in this work, NiO nanocrystals loaded on the tunable CeO_2 crystal facets ({110}, {111} and {100} facets) were effectively synthesized. The obtained NiO/CeO_2 catalysts with three shapes were characterized in detail by X-ray diffraction (XRD), transmission electron microscopy (TEM), N_2-physisorption, UV-Vis diffuse reflectance spectra (DRS), X-ray photoelectron spectroscopy (XPS), temperature-programmed reduction (TPR), and *in-situ* diffuse reflectance infrared Fourier transform spectra (DRIFTS). The study was mainly focused on: (1) the crystal-plane effects of CeO_2 supports on the properties of NiO/CeO_2 catalysts; (2) investigating the interfacial structures between NiO and different-shaped CeO_2 nanocrystals by the incorporation model; (3) exploring the key factors which had the significant influence on the reactivity of CO oxidation. This study could provide a scientific basis on ceria-based catalysts CO oxidation by the effective interface design.

2. EXPERIMENTAL SECTION

2.1. Catalyst preparation

The nano-CeO_2 supports were synthesized following an approach by hydrothermal method.[17] In the preparation of CeO_2 nanorods, the desired amount of $CeCl_3 \cdot 7H_2O$

(0.75 g) was dissolved in 40 mL NaOH (9.6 g) aqueous solution. This stock solution was stirred vigorously for 30 min in a Teflon bottle, and the mixture was carried out under hydrothermal treatment at 140 ^{o}C for 18 h. After cooling, the precipitate was collected, washed with deionized water until the chloride ions were removed and pH=7, and dried at 60 ^{o}C overnight. The samples were calcined in air at 450 ^{o}C for 3 h.

In the preparation of CeO_2 nanooctahedron, the desired amount of $Ce(NO_3)_3$ $6H_2O$ (0.44 g) was dissolved in the mixture of toluene (15mL) and H_2O (25mL), and then 0.15 mL butylamine was dropped. The above mixture was stirred vigorously for 30 min in a Teflon bottle, and carried out under hydrothermal treatment at 180 ^{o}C for 24 h. The obtained precipitate was washed with deionized water until pH=7, and dried at 60 ^{o}C overnight. The samples were calcined in air at 450 ^{o}C for 3 h.

In the preparation of CeO_2 nanocubes, the desired amount of $Ce(NO_3)_3$ $6H_2O$ (0.87 g) was dissolved in 40 mL NaOH (9.6 g) aqueous solution. This stock solution was stirred vigorously for 30 min in a Teflon bottle, and the mixture was carried out under hydrothermal treatment at 180 ^{o}C for 24 h. The obtained precipitate was treated in the similar way as the case of octahedron.

The NiO/CeO_2 catalysts were prepared by the wet impregnation method with a solution containing $Ni(NO_3)_2$. The mass ratio of $NiO:CeO_2$ = 3 wt%. The mixture was stirred for 7 h at room temperature, and the solvent was evaporated at 100 ^{o}C. The resulting powder was dried overnight at 110 ^{o}C, and calcined at 350 ^{o}C in air for 3 h. The obtained NiO/CeO_2 rod, octahedron and cube were denoted as Ni/CeO_2-r, Ni/CeO_2-o and Ni/CeO_2-c, respectively.

2.2. Catalyst characterization

Transmission electron microscopy (TEM) images were taken on a JEM-2100 instrument at an acceleration voltage of 200 kV. The samples were crushed and dispersed in A.R. grade ethanol and the resulting suspensions were allowed to dry on carbon film supported on copper grids. The crystal structure of three Ni/CeO_2 catalysts were identified by X-ray diffraction (XRD) with a Philips X'Pert Pro

diffractometer using Ni-filtered Cu Kα radiation (λ = 0.15418 nm). Brunauer–Emmet–Teller (BET) surface areas were measured by nitrogen adsorption at 77 K on a Micrometrics ASAP-2020 adsorption apparatus. Before each adsorption measurement, approximate 0.1 g sample was degassed in a N_2/He mixture at 200 ^oC for 3 h. UV-Vis diffuse reflectance spectroscopy (UV-vis DRS) were recorded in the range of 200–800 nm by a Shimadzu UV-2401 spectrophotometer with $BaSO_4$ as reference. Laser Raman spectra (LRS) were collected on a Renishaw invia Laser Raman spectrometer using Ar+ laser beam. The Raman spectra were recorded with an excitation wavelength of 532 nm and the laser power of 20 mW. The X-ray tube was operated at 40 kV and 40 mA. X-ray photoelectron spectroscopy (XPS) analysis were performed on a PHI 5000 VersaProbe high performance electron spectrometer, using monochromatic Al Kα radiation (1486.6 eV), the sample was outgassed at room temperature in a UHV chamber ($< 5 \times 10^{-7}$ Pa). The sample charging effects were compensated by all binding energies (BE) referenced to the C 1s peak at 284.6 eV. This reference gave BE values with an error within ±0.1 eV. H_2-temperature programmed reduction (H_2-TPR) experiments were performed with H_2 as a reduced agent in a quartz U-type reactor, and about 50 mg sample was used for each measurement. Prior to the reduction, the sample was pretreated in a highly purified N_2 stream at 200 ^oC for 30 min and then cooled to ambient temperature. H_2-Ar mixture (7% H_2 by volume) was switched on, the temperature increased with a ramp of 5 ^oC/min. The consumption of H_2 was monitored on line by a thermal conductivity detector. *In-situ* diffuse reflectance infrared Fourier transform spectra (*in-situ* DRIFTS) were collected from 1000 to 4000 cm^{-1} at a spectral resolution of 4 cm^{-1} (number of scans, 32) on a Nicolet 5700 FT-IR spectrometer equipped with a high-sensitive MCT detector cooled by liquid N_2. The DRIFTS cell (Harrick) was fitted with a ZnSe window and a heating cartridge that allowed sample to be heated to 400 ^oC. The fine catalyst powder placed on a sample holder was carefully flattened to enhance IR reflection. The sample was purged with a high purified N_2 stream from room temperature to 400 ^oC at 10 ^oC/min to eliminate the physisorbed water and other impurities. The sample background of each target temperature was collected during

the cooling process. At ambient temperature, the sample was exposed to a controlled stream of CO-Ar (10% of CO by volume) and O_2 at a rate of 5.0 ml/min for 30 min to be saturated. Reaction studies were performed by heating the adsorbed species and the spectra were recorded at various target temperatures at a rate of 10 ^oC/min from room temperature to 250 ^oC by subtraction of the corresponding background reference. The CeO_2 crystal structures were drawn using the Materials Studio 6.0 software.

2.3. Catalytic performances measurement

The CO oxidation activities of the catalysts were measured in a flow micro-reactor with a gas composition of 1.8 vol% CO, 10.0 vol% O_2 and 88.2 vol% N_2 at a space velocity of 40,000 mL g^{-1} h^{-1}, and 50 mg catalyst was used for each measurement. The catalyst was pretreated in a N_2 stream at 200 ^oC for 30 min and then cooled to room temperature, after that, the mixed gases were switched on. Two columns and thermal conductivity detector (TCD) were used for the purpose of analyzing the production, column A with 13× molecular sieve for separating O_2, N_2 and CO, and column B, packed with Porapak Q for separating CO_2.

In the kinetic study, approximately 10 mg of catalyst was carried out in sequential measurements (the conversion of CO was below 20%). The turnover frequency (TOF) for CO conversion to CO_2 was calculated in a following equation TOF = $PV_s\eta V_{CO}\%/RTn_{Ni}$ (P = atmospheric pressure, Vs = space velocity, η = CO conversion, V_{CO}% = CO concentration, n_{Ni} = the moles of surface NiO determined by XPS).

3. RESULTS AND DISCUSSION

3.1. Morphology characterizations (TEM and high resolution TEM)

TEM was performed to determine the morphologies of as-synthesized CeO_2 nanocrystals. As shown in **Figure S1** (in Supporting Information), these particles had the uniform shapes. Nanorods with the length of 70-100 nm and the diameter of *ca.* 10 nm were displayed in **Figure S1a**, and the lattice spacing of 0.19 and 0.27 nm suggested that nanorods preferred to expose {110} and {100} facets (**Figure S1b**).

Nanooctahedrons and cubes with the average size of 30 nm were mainly exposed {111} and {100} facets, respectively (**Figure S1c-f**).

The morphologies of Ni/CeO_2 samples were determined in **Figure 1** and **Figure S2, 3**, suggesting that CeO_2 nanocrystals still kept the original shapes and unique crystal facets after the introduction of nickel oxide. Since the loading amount of NiO was low, the selected area electron diffraction technology was employed to catch the NiO particles. In **Figure 1a**, the different diffraction rings arose from the diffraction spots, which corresponded to CeO_2 (111), (200) and (220) planes, respectively (JCPDS65-2975). While, for the selected area electron diffraction of Ni/CeO_2 rod (**Figure 1b**), besides the above diffraction rings corresponding to CeO_2, some weak diffraction spots were observed, which was ascribed to the NiO (200) plane (JCPDS78-0643). The white contrast in the dark field image (**Figure 1c**) came from the selection of electrons, which were diffracted by the crystal planes of NiO nanocrystals with respect to the incident beam.[21,22] Moreover, the corresponding bright field image was showed in **Figure 1d**. Compared the bright field with the dark field images (**Figure 1c and d**), the approximate location of NiO nanoparticles was found, and the HRTEM result of Ni/CeO_2 rod was displayed in **Figure 1e**. The lattice spacing of 0.20 nm was ascribed to the NiO (200) crystal plane, and the lattice spacing of 0.19, 0.26 nm are ascribed to the CeO_2 (220) and (200) crystal planes, respectively. Similarly, the selected area electron diffraction, dark field, bright field and HRTEM images of Ni/CeO_2 octahedron and cube were showed in **Figure S2** and **S3**, respectively. From the above images, NiO nanoparticles could be found, and the interface between NiO and CeO_2 (rod, octahedron, cube) were clearly displayed. Therefore, it was concluded that the obtained Ni/CeO_2 samples with different CeO_2 crystal facets were ideal model catalysts to investigate the crystal-plane effect on catalytic performance.

3.2. Catalytic tests of CO oxidation

CO oxidation was employed as the model reaction to assess the activity of Ni/CeO_2 and CeO_2 with different morphologies. **Figure S4** suggested that the activities of different-shaped CeO_2 were in the following order: CeO_2-r > CeO_2-o > CeO_2-c. When

NiO were loaded on the three CeO_2 supports, the CO oxidation performances were significantly enhanced (**Figure 2a**). Moreover, the obtained Ni/CeO_2 catalysts displayed different activities. Ni/CeO_2-r {110} catalysts showed the superior activity: 100% CO conversion was achieved at 130 ^oC, while, for Ni/CeO_2-o {111} and Ni/CeO_2-c {100}, the temperatures were 160 and 190 ^oC, respectively. The CO oxidation activities were ranked by Ni/CeO_2-r {110} > Ni/CeO_2-o {111} > Ni/CeO_2-c {100}. The kinetic data were further confirmed that Ni/CeO_2-r {110} was the best catalyst. The activation energies were ranked by: Ni/CeO_2-r (55.4 kJ/mol) < Ni/CeO_2-o (68.2 kJ/mol) < Ni/CeO_2-c (88.7 kJ/mol) (**Figure 2b**). The turnover frequency numbers at 120 ^oC for CO conversion over per mole of NiO were ranked by Ni/CeO_2-r (35.2 h^{-1}) > Ni/CeO_2-o (10.1 h^{-1}) > Ni/CeO_2-c (0.5 h^{-1}) (**Table S1**).

On the basis of the above results, it could be deduced that NiO nanoclusters on different CeO_2 crystal facets formed the different Ni/CeO_2 interfaces, and then the interfacial structures exerted an effect on the properties of Ni/CeO_2 samples. Therefore, the obtained samples were characterized in detail to reveal the relationships.

3.3. Structural and textural characterizations (XRD, Raman and N_2-physisorption)

XRD patterns indicated that CeO_2 nanorod, nanooctahedron and nanocube were the pure cubic phase with the fluorite structure (JCPDS65-2975, space group Fm3m), and the lattice parameters were 5.4133, 5.4064, and 5.4022 Å, respectively (**Figure S5**). After the introduce of nickel oxide species, the three CeO_2 maintained the original face-centered cubic structure, no other nickel oxide species could be detected in this pattern, suggesting that the NiO species were well dispersed.[23] However, the lattice parameters of ceria decreased when ceria was supported by NiO (in **Table S1**), which in turn confirmed that partial Ni^{2+} ions might be incorporated into the surface layer of CeO_2 supports. In addition, the decreased degree of three Ni/CeO_2 samples were different in comparison with the bare CeO_2, implying the structures of nickel species on the surface layers of ceria were various.

The surface structure information of the Ni/CeO_2 samples was further investigated by Raman spectroscopy. An obvious peak at 460 cm^{-1} corresponded to the Raman

active F_{2g} vibration model of the CeO_2 fluorite structure and two weak bands ~ 600 and 1170 cm^{-1} related to the presence of oxygen defects were displayed in **Figure 3**.[24] The absence of characteristic bands for NiO crystallite phase implied the well-dispersion of NiO, consistent with XRD results. Evidently, the F_{2g} vibration peak was red-shifted in Ni/CeO_2-r, indicating that the stronger interfacial interaction decreased the symmetry of the Ce-O bond. The surface oxygen defect concentration determined by $I_{605+1172}/I_{460}$ (**Table S1**) was followed the sequence of Ni/CeO_2-r > Ni/CeO_2-o > Ni/CeO_2-c > CeO_2-r > CeO_2-o > CeO_2-c. On the basis of the above discussion, it was deduced that the interface structures between NiO and CeO_2 {110} decreased the bond strength of Ce−O bond and then enhanced the surface oxygen defect concentration, which might result in the superior reactivity of CO oxidation. In addition, the textural properties of the prepared Ni/CeO_2 and CeO_2 samples were studied by N_2 adsorption–desorption isotherms (**Figure S6**). The surface area results in **Table S1** seemed to have little relationship with the reactivity, and thus it was not the key factor for the catalytic performance of CO oxidation.

3.4. Chemical states analysis (UV-Vis DRS and XPS)

The information of the surface electronic states could be found out from UV-Vis DRS characterization. In **Figure 4**, different-shaped CeO_2 samples exhibited a peak at 323 nm corresponding to an $O^{2-}\rightarrow Ce^{4+}$ charge transfer and a broad absorption edge of CeO_2.[25] While, for Ni/CeO_2 samples, a weak peak at 220 nm was attributed to an $O^{2-}\rightarrow Ce^{3+}$ charge transfer,[17] due to the fact that partial interfacial Ni^{2+} ions were incorporated into the surface layer of CeO_2, the redox equilibrium ($Ni^{2+}+Ce^{4+}\rightarrow Ni^{3+}+Ce^{3+}$) shifted to the right, and then Ce^{3+} species were generated. Another peak at around 735 nm was the d-d bands of octahedrally coordinated Ni^{2+}.[25,26] It was observed that the peak of Ni/CeO_2-r was blue-shifted and weakened, further suggesting that interfacial interaction between NiO and CeO_2 {110} affected the electronic structures of surface nickel species.

In order to exhaustively explore the surface compositions and elementary oxidation states of Ni/CeO_2 samples with different shaped, XPS technique was carried out and the corresponding results were displayed in **Figure 5**. The Ce 3d spectra of these

samples were fitted into eight peaks as defined in **Figure 5a**. On the basis of the literatures, the peaks labeled as u′ and v′ represented Ce^{3+}, and the other six peaks labeled as u‴ and v‴, u″ and v″, u and v were corresponding to Ce^{4+}.[27-29] The content ratio of Ce^{3+} to Ce^{4+} over Ni/CeO_2 and CeO_2 samples were calculated in **Table 1**. It could be observed that the introduce of NiO enhanced the amount of Ce^{3+} species, and the content of Ce^{3+} in Ni/CeO_2-r was the highest among Ni/CeO_2 samples. Moreover, it was well-known that the surface oxygen activation was the key factor for CO oxidation, and then the O 1s information was measured (**Figure S7**). The main peak labeled as O′ at 529.1 eV was the lattice oxygen in metal oxide, and a shoulder labeled as O″ at 531.5 eV was attributed to the adsorbed oxygen (oxygen in hydroxyl, carbonates groups).[30] The ratios of O″/O′ for Ni/CeO_2 and CeO_2 samples suggested that more active oxygen was adsorbed on Ni/CeO_2 surface and Ni/CeO_2-r was the best for the surface active oxygen adsorption, confirmed by the result of O/(Ni+Ce) (**Table 1)**. The above phenomenon was mainly from Ce^{3+} species, which was beneficial for water and C-O species adsorption than Ce^{4+} species.[31,32]

In addition, the valence state of nickel species was also investigated, and the Ni 2p spectra were exhibited in **Figure 5b.** A main peak centered at *ca.* 854.9 eV was assigned to Ni^{2+} species, with a broad shake-up satellite peak at *ca.* 861.0 eV.[33,34] The Ni^{2+} binding energy of Ni/CeO_2-r was higher, which indicated that the interface might make some electrons transfer from Ni^{2+} to Ce^{4+}, and then the Ce^{3+} and adsorbed oxygen species were increased, which led to the enhanced catalytic performance.

3.5. Reduction properties (H_2-TPR and in-situ CO-adsorption DRIFTS)

The reducibility of Ni/CeO_2 samples was estimated by H_2-TPR and *in-situ* CO-adsorption DRIFTS characterizations. The H_2-TPR results were showed in **Figure S8**, obviously, the reduction temperature of Ni/CeO_2 was lower than that of CeO_2, suggesting that the introduce of NiO was helpful for the migration of oxygen species. Furthermore, it was observed that the shapes of these TPR profiles over Ni/CeO_2 samples were distinct, suggesting that the migration of oxygen species were greatly dependent on the interfacial interactions of Ni/CeO_2 samples. The broad peak in **Figure 6** was fitted into three peaks (labeled as α β γ). According to literatures, the

peak at *ca.* 200 °C (α1, α2) attributed to the surface active adsorbed oxygen species.[35] The second peak (β) was the reduction of NiO species strongly interacted with CeO_2 supports. While, the third peak (γ) might come from the reduction of NiO clusters.[25] Among three Ni/CeO_2 samples, Ni/CeO_2-c sample had the poorest reducibility. In addition, the hydrogen consumption of the complete reduction of Ni^{2+} to Ni^0 over three Ni/CeO_2 samples were displayed in comparison (**Table 1)**. It could be found that the actual hydrogen consumption was much higher than the theoretical value (388 μmol•g^{-1}), for the reason that the surface oxygen species from CeO_2 was reduced with NiO reduction.[17] Notably, the actual H_2 consumption of Ni/CeO_2-r was approximately two times higher than that of Ni/CeO_2-c, illustrating that the geometric and electronic structures of nickel species were relying on the interfacial interactions of Ni/CeO_2 samples. The interfacial between nickel species and CeO_2 {110} was advantageous for the improved oxygen species migration and reducibility.

To further understand the reduction properties of Ni/CeO_2 catalysts, *in situ* CO-adsorption DRIFT as a probe reaction was carried out in a TPR procedure, the related results were present (**Figure S9**). The band at *ca.* 2170 cm^{-1} from the CO adsorption on Ni species and bands at 1000-1800 cm^{-1} for the vibration of carbonates[36] were obvious for Ni/CeO_2-r, suggesting that Ni/CeO_2-r was facilitate for the adsorption and activation of CO. Moreover, with the increase of temperature, a peak centered at *ca.* 2358 cm^{-1} of gaseous CO_2 appeared,[31,35] indicating the surface species of oxides started to reduce. The initial reduction temperatures were ranked by Ni/CeO_2-r ≈ Ni/CeO_2-o < Ni/CeO_2-c, and the initial reduction temperature was lower than that of H_2-TPR, for the reason that the DRIFT method was very sensitive to surface process.[5] On the basis of the above analysis, it was suggested that the interfaces between NiO and CeO_2 rod {110} were more beneficial for CO adsorption and activation, which was an important factor for CO oxidation.

3.6. Proposed mechanism of CO oxidation and interfacial model of Ni/CeO_2 catalysts (in-situ DRIFTS of CO and O_2 co-adsorption)

In order to explore the surface reaction situation of Ni/CeO_2 catalysts with different crystal planes, CO and O_2 co-adsorption *in-situ* DRIFTS were recorded at various

temperatures in the simulated reaction conditions, the results were displayed in **Figure 7**. Hydroxyl species was detected in the range from *ca.* 3700 to 3000 cm^{-1}. It was reported that the band at *ca.* 3650 cm^{-1} was assigned to OH coordinated on Ce^{3+} sites, whereas, the band at *ca.* 3300 cm^{-1} was assigned to OH coordinated on Ce^{4+} sites.[18,37] It was worth noting that hydroxyl groups were more apparent for Ni/CeO_2-r, followed by Ni/CeO_2-o; conversely, the intensity of the hydroxyl species bands was negligible in the Ni/CeO_2-c. With the increase of temperatures, the OH band was disappeared, which indicated that the OH sites participated in CO oxidation, consistent with our previous work, i.e., OH species played an role.[15] Therefore, Ni/CeO_2-r had the superior catalytic performance, because the advantageous interfacial interactions could active the substrate molecules of hydroxyl species.

On the other hand, the formation of carboxylate, carbonate and other related species were comprehensively analyzed. Based on the literature, the bands at *ca.* 2926, 2863, 1600, 1300 cm^{-1} were ascribed to carboxylate ions, the C–H stretching, the antisymmetric and symmetric stretching vibration (ν_{as} and ν_s) of formate species.[38,39] The intensity of formate species band was ranked by Ni/CeO_2-r $\approx$ Ni/CeO_2-o > Ni/CeO_2-c. With the increase of temperatures, the intensity of formate species was decreased, while, the carbonate species (1530 and 1390 cm^{-1} for monodentate carbonates; 1470 and 880 cm^{-1} for carbonites)[40,41] and CO_2 (2358 cm^{-1}) were generated. With the higher temperature, the carbonate species were decreased. It was observed that carbonate species on Ni/CeO_2-c were difficult to desorbed, which was proposed to decrease the activity.[42] On the basis of the above discussion, it was deduced that the important intermediate formate species was resulted from the synergetic interaction of adsorbed OH and CO species. The OH species was from the active oxygen species on surface, and the CO molecule was from the adsorption on interfacial nickel species. Both the two factors for CO oxidation were related to the geometric and electronic structures of nickel species on CeO_2 crystal planes. Therefore, a tentative model of interfacial nickel oxide species on the CeO_2 (110), (111) and (100) surface layers was proposed as followed.

According to our previous incorporation model,[43] it was deduced that the nickel

species on interface were incorporated in different vacancy sites of CeO_2 {110} {111} {100} surface layers, and the interfacial structures of nickel species were proposed (**Figure 8**). On Ni/CeO_2 {110} interface, the nickel species were surrounded by four lattice oxygen atoms in a square structure; on Ni/CeO_2 {111} interface, that were surrounded by four lattice oxygen atoms in a trigonal pyramid structure; whereas, on Ni/CeO_2 {100} interface, that were surrounded by eight lattice oxygen atoms in a hexahedron structure. Due to the steric effect, the Ni/CeO_2 {110} interface was helpful for CO adsorption and activation. This similar phenomenon of steric effect was also observed in the report about CO adsorption on different-shaped Cu_2O.[44] In a word, the interfacial structures of nickel species on CeO_2 surface layers could not only affect the adsorption and activation of reactant CO on nickel species, but also modify the surface oxygen atoms migration of CeO_2, which had influences on the catalytic property of CO oxidation.

Moreover, the possible reaction process was described as followed: CO firstly adsorbed and activated on interfacial nickel species, and then reacted with the surrounding active oxygen species to generate the formate species, finally the formate species was decomposed to CO_2 and carbonate species at relatively high temperature. In the process, the adsorption/activation of CO, the form of active surface oxygen species and formate species, and desorption of carbonate species were highly dependent on Ni/CeO_2 interface.

4. CONCLUSIONS

In this work, it was showed that the catalytic properties were markedly resulted from the geometric and electronic structures of NiO/CeO_2 interface. NiO nanoparticles loaded on tunable CeO_2 crystal facets ({110}, {111} and {100} facets) were synthesized. Kinetic studies of CO oxidation demonstrated that the catalytic performances of three prepared NiO/CeO_2 samples followed this order: NiO/CeO_2 {110} > NiO/CeO_2 {111} > NiO/CeO_2 {100}. With the help of XRD, Raman, UV-Vis DRS, XPS and TPR characterizations, it was showed that the interaction

($Ni^{2+}+Ce^{4+}\rightarrow Ni^{3+}+Ce^{3+}$) was present on the interface and then more Ce^{3+} and surface active oxygen species were generated. The reaction process was explored by *in-situ* DRIFTS, it was proposed that CO firstly adsorbed and activated by the interfacial nickel species, and then reacted with the surrounding active oxygen species to generate the formate species, finally the formate species was decomposed to CO_2 and carbonate species at relatively high temperature. The important intermediate formate species was related with the geometric and electronic structures of nickel species on interface. Due to the advantageous NiO/CeO_2 {110} interface, it was helpful for CO adsorption/activation and the generation of surface active oxygen species, which played the key role in CO oxidation. Considering of their different interfacial structures, it was believed that tuning the crystal facets of CeO_2 supports would be an effective strategy to enhance the reactivity of ceria-based catalysts.

ACKNOWLEDGMENT

Financial supports from the Doctoral Fund of Ministry of Education of China (No.2013009111005), Jiangsu Province Science and Technology Support Program (Industrial, BE2014130), Natural Science Foundation of Jiangsu Province (BK2012298) and National Natural Science Foundation of China (Nos.21273110, 21203091) are gratefully acknowledged.

REFERENCES

1 L. Qi, Q. Yu, Y. Dai, C. J. Tang, L. J. Liu, H. L. Zhang, F. Gao, L. Dong, Y. Chen, *Appl. Catal. B: Environ.* **2012**, *119-120*, 308-320.

2 C. W. Sun, H. Li, L. Q. Chen, *Energy Environ. Sci.* **2012**, *5*, 8475-8505.

3 B. M. Weckhuysen, M. P. Rosynek, J. H. Lunsford, *Phys. Chem. Chem. Phys.* **1999**, *1*, 3157-3162.

4 E. Mamontov, T. Egami, R. Brezny, M. Koranne, S. Tyagi, *J. Phys. Chem. B* **2000**, *104*, 11110-11116.

5 X. J. Yao, Y. Xiong, W. X. Zou, L. Zhang, S. G. Wu, X. Dong, F. Gao, Y. Deng, C.

J. Tang, Z. Chen, L. Dong, Y. Chen, *Appl. Catal. B: Environ.* **2014**, *144*, 152-165.

6 J. M. López, A. L. Gilbank, T. García, B. Solsona, S. Agouram, L. Torrente-Murciano, *Appl. Catal. B: Environ.* **2015**, *174-175*, 403-412.

7 C. M. Ho, J. C. Yu, T. Kwong, A. C. Mak, S. Y. Lai, *Chem. Mater.* **2005**, *17*, 4514-4522.

8 Q. Yuan, H. H. Duan, L. L. Li, L. D. Sun, Y. W. Zhang, C. H. Yan, *J. Colloid Interf. Sci.* **2009**, *335*, 151-167.

9 H. X. Mai, L. D. Sun, Y. W. Zhang, R. Si, W. Feng, H. P. Zhang, H. C. Liu, C. H. Yan, *J. Phys. Chem. B* **2005**, *109*, 24380-24385.

10 D. C. Sayle, S. A. Maicaneanu, G. W. Watson, *J. Am. Chem. Soc.* **2002**, *124*, 11429-11439.

11 T. S. Sreeremya, A. Krishnan, K. C. Remani, K. R. Patil, D. F. Brougham, S. Ghosh, *ACS Appl. Mater. Inter.* **2015**, *7*, 8545-8555.

12 X. Wang, Z. Y. Jiang, B. J. Zheng, Z. X. Xie, L. S. Zheng, *CrystEngComm* **2012**, *14*, 7579-7582.

13 Z. L. Wu, M. J. Li, S. H.Overbury, *J. Catal.* **2012**, *285*, 61-73.

14 Y. Bai, W. H. Zhang, Z. H. Zhang, J. Zhou, X. J. Wang, C. M. Wang, W. X. Huang, J. Jiang, Y. J. Xiong, *J. Am. Chem. Soc.* **2014**, *136*, 14650-14653.

15 L. C. Liu, X. R. Gu, Y. Cao, X. J. Yao, L. Zhang, C. J. Tang, F. Gao, L. Dong, *ACS Catal.* **2013**, *3*, 2768-2775.

16 R. Si, M. Flytzani-Stephanopoulos, *Angew. Chem. Int. Ed.* **2008**, *47*, 2884-2887.

17 L. J. Liu, Z. J. Yao, Y. Deng, F. Gao, B. Liu, L. Dong, *ChemCatChem* **2011**, *3*, 978-989.

18 E. T. Saw, U. Oemar, X. R. Tan, Y. Du, A. Borgna, K. Hidajat, S. Kawi, *J. Catal.* **2014**, *314*, 32-46.

19 J. S. Elias, M. Risch, L. Giordano, A. N. Mansour, Y. Shao-Horn, *J. Am. Chem. Soc.* **2014**, *136*, 17193-17200.

20 H. B. Zhou, P. L. Hu, Z. Huang, F. Qin, W. Shen, H. L. Xu, *Ind. Eng. Chem. Res.* **2013**, *52*, 4504-4509.

21 S. Schamm, C. Bonafos, H. Coffin, N. Cherkashin, M. Carrada, G. Ben Assayag,

A. Claverie, M. Tence, C. Colliex, *Ultramicroscopy* **2008**, *108*, 346-355.

22 I. Crupi, S. Lombardo, C. Spinella, C. Bongiorno, Y. Liao, C. Gerardi, B. Fazio, M. Vulpio, S. Privitera, *J. Appl. Phys.* **2001**, *89*, 5552-5559.

23 P. Maitarad, J. Han, D. S. Zhang, L. Y. Shi, S. Namuangruk, T. Rungrotmongkol, *J. Phys. Chem. C* **2014**, *118*, 9612-9620.

24 X. J. Du, D. S. Zhang, L. Y. Shi, R. H. Gao, J. P. Zhang, *J. Phys. Chem. C* **2012**, *116*, 10009-10016.

25 S. K. Mahammadunnisa, P. Manoj Kumar Reddy, N. Lingaiahb, Ch. Subrahmanyam, *Catal. Sci. Technol.* **2013**, *3*, 730-736.

26 P. V. R. Rao, V. P. Kumar, G. S. Rao, K. V. R. Chary, *Catal. Sci. Technol.* **2012**, *2*, 1665-1673.

27 V. M. Shinde, G. Madras, *Appl. Catal. B: Environ.* **2013**, *138*, 51-61.

28 P. Hartmann, T. Brezesinski, J. Sann, A. Lotnyk, J. P. Eufinger, L. Kienle, J. Janek, *ACS Nano* **2013**, *7*, 2999-3013.

29 Z. L. Wu, M. J. Li, J. Howe, H. M. Meyer, S. H. Overbury, *Langmuir* **2010**, *26*, 16595-16606.

30 A. Velamakanni, K. J. Ganesh, Y. W. Zhu, P. J. Ferreira, P. S. Ruoff, *Adv. Funct. Mater.* **2009**, *19*, 3926-3933.

31 X. J. Yao, Q. Yu, Z. Y. Ji, Y. Y. Lv, Y. Cao, C. J. Tang, F. Gao, L. Dong, Y. Chen, *Appl. Catal. B: Environ.* **2013**, *130-131*, 293-304.

32 R. K. Pati, I. C. Lee, S. Hou, O. Akhuemonkhan, K. J. Gaskell, Q. Wang, A. I. Frenkel, D. Chu, L. G. Salamanca-Riba, S. H. Ehrman, *ACS Appl. Mater. Inter.* **2009**, *1*, 2624-2635.

33 E. Heracleous, A. F. Lee, K. Wilson, *J. Catal.* **2005**, *231*, 159-171.

34 D. Y. Kim, J. Ryu, J. Manders, J. Lee, F. So, *ACS Appl. Mater. Inter.* **2014**, *6*, 1370-1374.

35 W. Q. Xu, Z. Y. Liu, A. C. Johnston-Peck, S. D. Senanayake, G. Zhou, D. Stacchiola, E. A. Stach, J. A. Rodriguez, *ACS Catal.* **2013**, *3*, 975-984.

36 J. P. Holgado, F. Ternero, V. M. Gonzalez-delaCruz, A. Caballero, *ACS Catal.* **2013**, *3*, 2169-2180.

37 C. Binet, M. Daturi, J. C. Lavalley, *Catal. Today* **1999**, *50*, 207-215.

38 F. Boccuzzi, A. Chiorino *J. Phys. Chem.* **1996**, *100*, 3617-3626.

39 J. Huang, C. J. Xue, B. F. Wang, X. Z. Guo, S. R. Wang, *Reac. Kinet. Mech. Cat.* **2013**, *108*, 403-416.

40 N. Gupta, V. Kamble, R. Iyer, K. Ravindranthan, K. Thampi, M. Grätzel, *J. Catal.* **1992**, *157*, 473-483.

41 N. Babaeva, A. Tsyganenko, *J. Catal.* **1990**, *123*, 396-407.

42 Z. Ren, Z. L. Wu, W. Q. Song, W. Xiao, Y. B. Guo, J. Ding, S. L. Suib, P. X. Gao, *Appl. Catal. B: Environ.* **2016**, *180*, 150-160.

43 L. Dong, Y. H. Hu, F. Xu, D. Lu, B. Xu, Z. Hu, Y. Chen, *J. Phys. Chem. B* **2000**, *104*, 78-85.

44 Q. Hua, T. Cao, H. Z. Bao, Z. Q. Jiang, W. X. Huang *ChemSusChem* **2013**, *6*, 1966-1972.

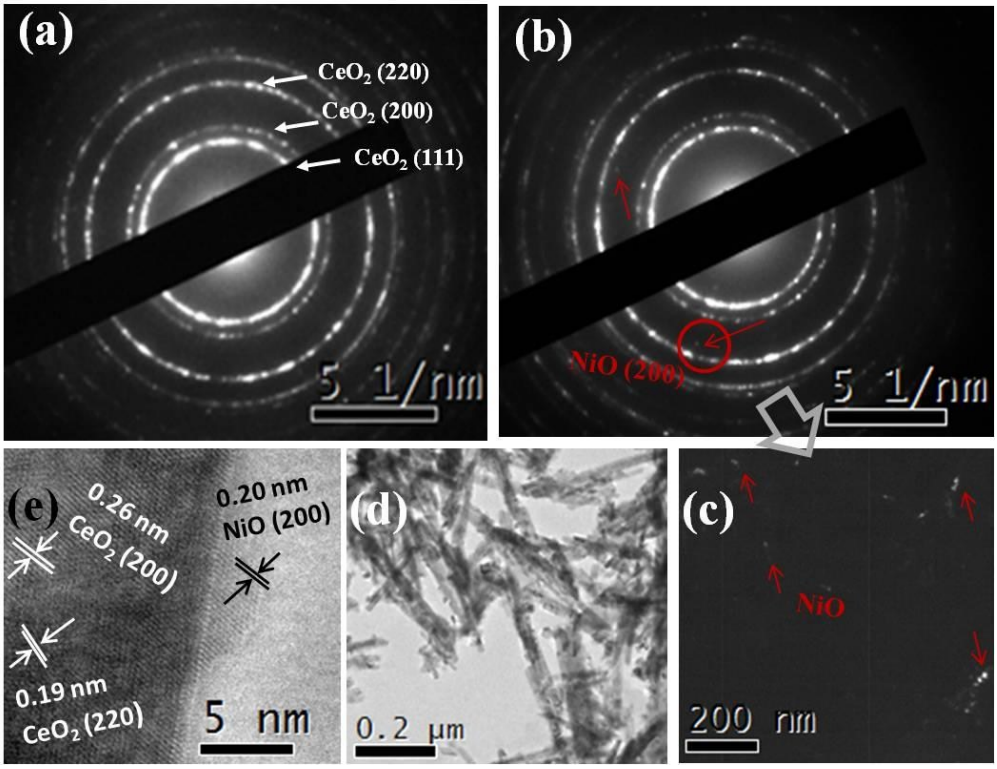

Figure 1. Electron diffraction patterns of (a) CeO_2 rod, (b) Ni/CeO_2 rod; (c) the corresponding dark field image of white spot in the red circle; (d) the corresponding bright field image; (e) the HRTEM image of Ni/CeO_2 rod.

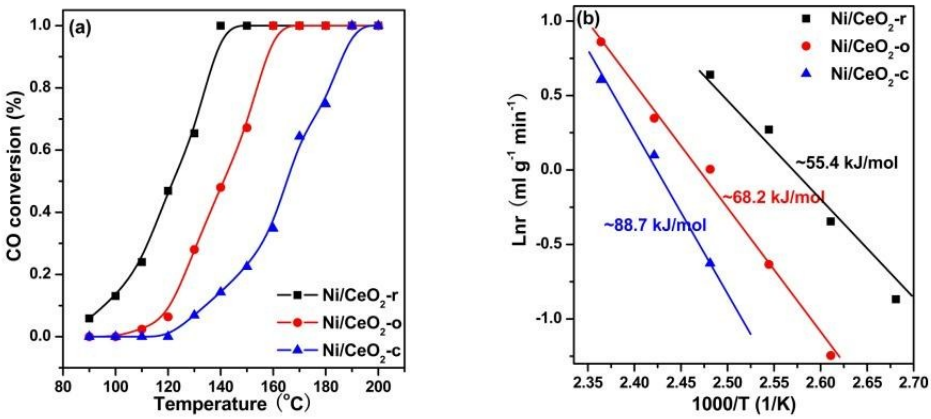

Figure 2. (a) CO conversion; (b) Arrhenius plots for CO conversion over Ni/CeO_2 catalysts with different shapes.

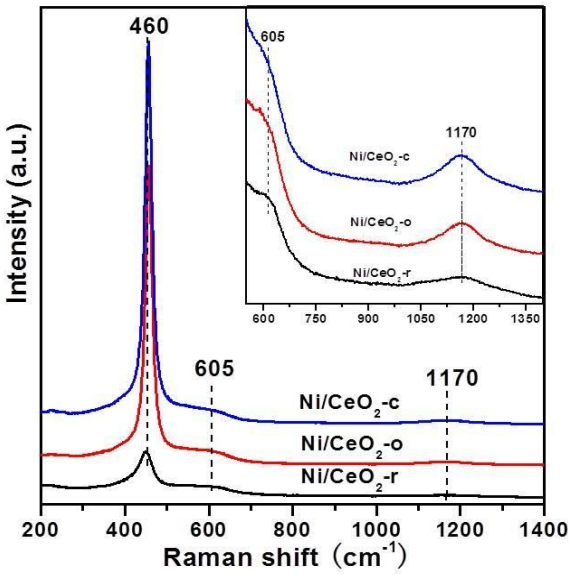

Figure 3. Raman results of Ni/CeO_2 catalysts with different shapes.

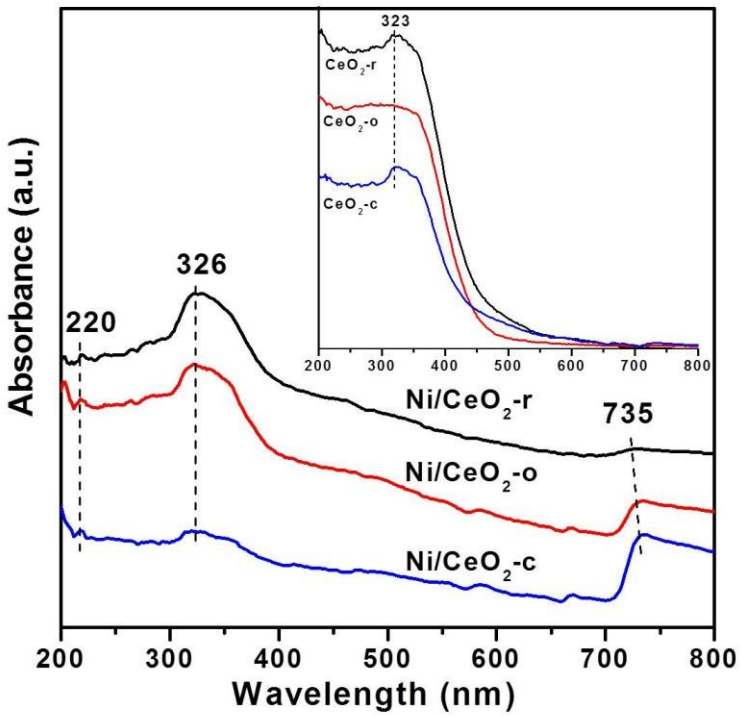

Figure 4. UV-vis DRS of Ni/CeO_2 and CeO_2 (insert graph) samples with different shapes.

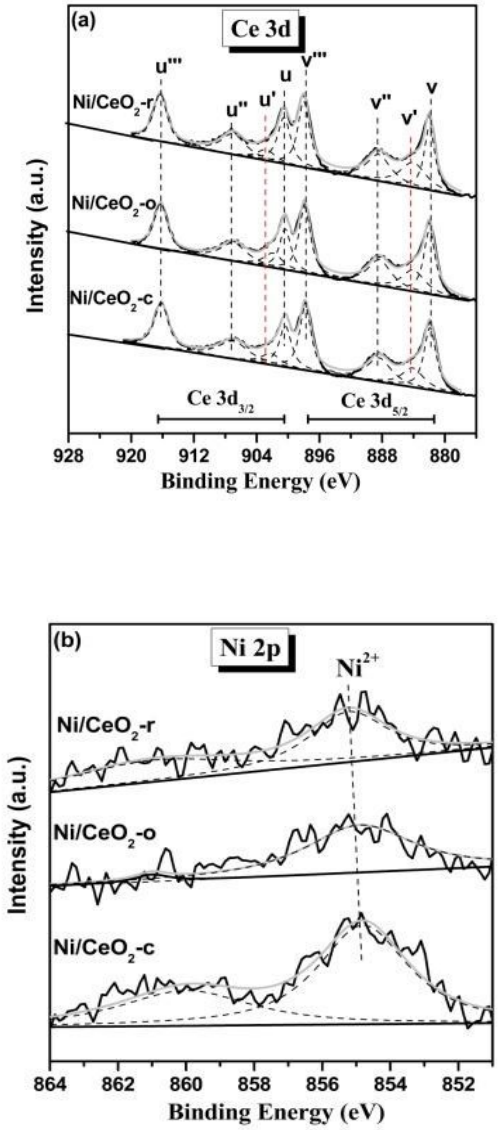

Figure 5. XPS spectra (a) Ce 3d and (b) Ni 2p of Ni/CeO_2 samples with different shapes.

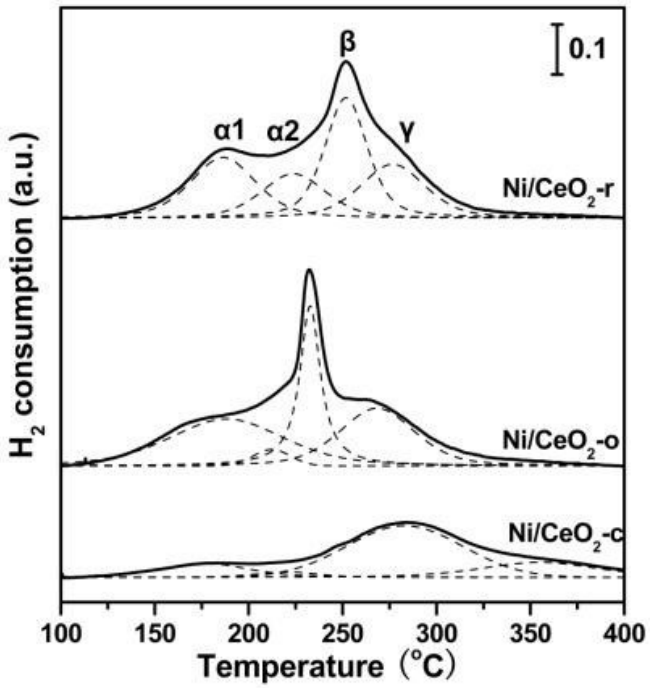

Figure 6. H_2-TPR profiles of Ni/CeO_2 with different shapes.

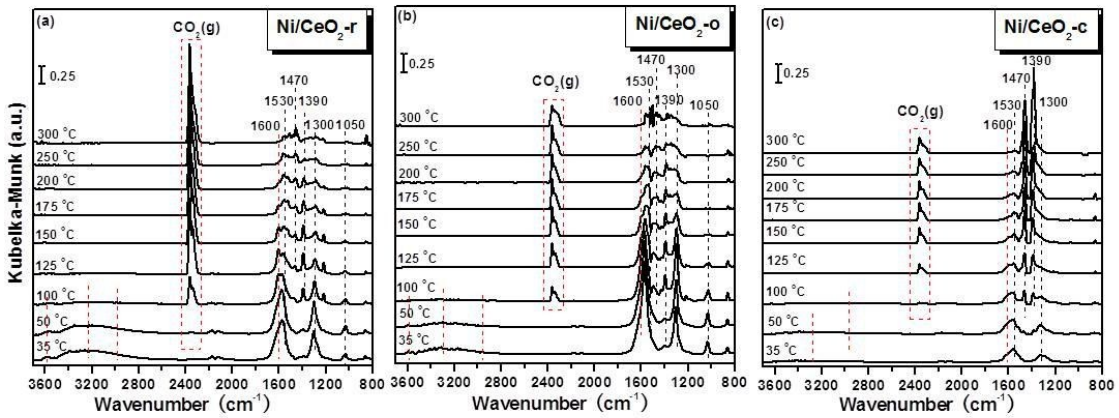

Figure 7. *In-situ* DRIFTS of CO and O_2 interaction with Ni/CeO_2 catalysts of different shapes.

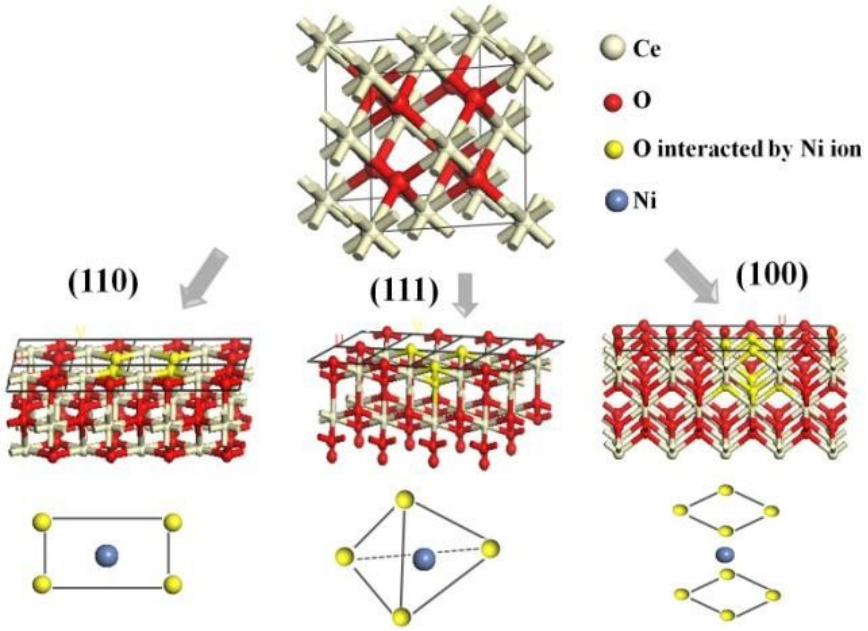

Figure 8. A tentatively proposed model of interfacial nickel oxide species on CeO_2 (110), (111) and (100) surface layers.

Table 1. XPS information and the actual H_2 consumption (the reduction of Ni^{2+} to Ni^0) of Ni/CeO_2 samples.

Samples	Atomic ratio			The actual H_2 consumption (μmol g^{-1})			
	O/(Ni+Ce)	$S_{O''}/S_{O'}$	Ce^{3+}/Ce^{4+}	α	β	γ	Total amount
Ni/CeO_2-r	3.71	0.29	0.22	312	240	161	713
Ni/CeO_2-o	3.58	0.25	0.21	267	189	195	651
Ni/CeO_2-c	3.56	0.27	0.17	104	91	206	401
CeO_2-r	–	0.27	0.16			–	
CeO_2-o	–	0.24	0.15			–	
CeO_2-c	–	0.23	0.16			–	